Probing isospin symmetry in the (^{50}Fe, ^{50}Mn, ^{50}Cr) isobaric triplet via electromagnetic transition rates

M. M. Giles,[1] B. S. Nara Singh,[1,2,*] L. Barber,[1] D. M. Cullen,[1] M. J. Mallaburn,[1] M. Beckers,[3] A. Blazhev,[3] T. Braunroth,[3] A. Dewald,[3] C. Fransen,[3] A. Goldkuhle,[3] J. Jolie,[3] F. Mammes,[3] C. Müller-Gatermann,[3] D. Wölk,[3] K. O. Zell,[3] S. M. Lenzi,[4] and A. Poves[5]

[1]*School of Physics & Astronomy, Schuster Building, The University of Manchester, Manchester M13 9PL, United Kingdom*
[2]*School of Engineering and Computing, University of the West of Scotland, Paisley, PA1 2BE, United Kingdom*
[3]*Institut für Kernphysik, Universität zu Köln, Köln D-50937, Germany*
[4]*Dipartimento di Fisica e Astronomia dell'Università and INFN, Sezione di Padova, Via F. Marzolo 8, Padova I-35131, Italy*
[5]*Departamento de Física teórica and IFT, UAM-CSIC, Universidad Autónoma de Madrid, Madrid E-28049, Spain*

(Received 1 July 2018; published 26 April 2019)

Lifetimes of the $T = 1$ isobaric analog $I^\pi = 2^+$ states in ^{50}Mn and ^{50}Cr were measured simultaneously by employing the recoil distance Doppler-shift (RDDS) technique. The states were populated in a fusion-evaporation reaction with a ^{12}C beam on a ^{40}Ca target. An analysis of the data and the calculations from the present work, together with the available $B(E2 : 2^+ \rightarrow 0^+)$ data of the isobaric analog states in ^{50}Fe and ^{50}Cr, were used to study isospin symmetry in the three $A = 50$ isobaric nuclei. Shell-model calculations reproduce the magnitudes as well as the increasing trend of the $B(E2)$ data with increasing Z. To draw a firm conclusion on the level of isospin mixing in the triplet, a new precision measurement of the $2^+ \rightarrow 0^+$ transition rate in ^{50}Fe will be required.

DOI: 10.1103/PhysRevC.99.044317

I. INTRODUCTION

Self-conjugate nuclei occupy a special place in the Segré chart where isospin-symmetry breaking (ISB) at the sub-nucleon level can manifest itself in bulk nuclear properties. For example, the observed slight differences between the energies of the isobaric analog states can originate from ISB [1]. The associated Coulomb energy differences (CED) were extensively studied for $N \sim Z$ nuclei in the $A \sim 50$ and 70 regions [2–9]. The observed trends in the CED were used to study nuclear phenomena such as backbending, rotational alignments of nucleons, changes in deformation, correlations of pairs of particles, and the evolution of charge radii [2–4,6,7,9]. In addition to the Coulomb interaction, an isospin nonconserving interaction between nucleons was required to explain the CED, implying ISB [5,7,8,10].

Electromagnetic (EM) transition rates in nuclei can rigorously probe the associated nuclear wave functions and are subjected to additional constraints due to the selection rules for the transitions [11]. Therefore, lifetime data or reduced transition probabilities can be used to validate any conclusions drawn on ISB using CED data and to test models stringently. In the context of the present lifetime measurements of the 2^+ states decaying through $E2\,\gamma$-ray transitions, the matrix element

$$\sqrt{B(E2\uparrow)} = M_{\rm tot} = M^0 + \frac{M^1 T_z}{\sqrt{T(T+1)(2T+1)}}$$

has to be a linear function of $T_z = \frac{N-Z}{2}$ for isobaric nuclei with isospin-pure wave functions [12]. Here, M^0 and M^1 are the isoscalar and isovector matrix elements, respectively. In a $T_z = 0\, N = Z$ nucleus, the isospin $T = 0$ and $T = 1$ states may lie close in energy, providing favorable conditions for the wave functions to mix in isospin. For example, the first excited 2^+ state of $T = 1$ type in ^{50}Mn lies $\sim$1 MeV below the second known excited 2^+ state as shown in Fig. 1 [6]. If the last of these is of $T = 0$ type and isospin mixing occurs significantly between these two states, then it could cause a nonlinear relationship between $M_{\rm tot}$ and T_z for the $A = 50$ triplet. A compilation of data from several works designed to search for such nonlinearities in the $A = 22$, 26, 30, 34, 38, and 42 isobaric triplet nuclei is given in Ref. [12]. A significant deviation from a linear trend could be observed only for the $A = 38$ case.

Along the $N = Z$ line, the level of isospin mixing is expected to increase quadratically with proton number [13,14]. Consequently, higher Z nuclei should, in general, serve as better candidates to study ISB. However, the sensitivity of nuclear-structure properties to the level of isospin mixing may be masked by nuclear phenomena such as shape coexistence. Indeed, nuclei in the $A \sim 70$, $N \sim Z$ region exhibit shape coexistence and therefore the $A \sim 50$, $N \sim Z$ nuclei may well be better candidates to isolate and study isospin mixing [15]. Despite this expectation and a strong motivation to study ISB, the measurement of transitions rates in the $A \sim 50$ region have been extremely limited. This can be attributed to the low-production rates of these nuclei, which hamper high-precision measurements [16–21].

*Corresponding author: snarasingh@gmail.com

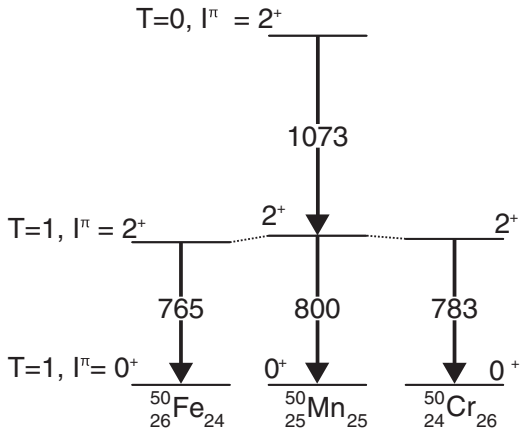

FIG. 1. A schematic representation of the $T = 1$, $2^+ \rightarrow 0^+ \gamma$-ray transition energies (in keV) in the $A = 50$ triplet. In ^{50}Mn, the known second 2^+ state at an excitation energy of 1873 keV is also shown with a tentative assignment of $T = 0$ along with the observed 1073-keV γ decay to the first $T = 1$, 2^+ state [6].

In the present work, the lifetimes of the isobaric analog first 2^+ states in ^{50}Mn and ^{50}Cr nuclei are measured simultaneously. The current result for ^{50}Cr is compared to the available precise data [16,17,19] to estimate any systematic uncertainties that might be present in our measurements. The lifetime of the 2^+ state in ^{50}Mn is obtained.The $B(E2 : 2^+ \rightarrow 0^+)$ value was previously measured for the analog 2^+ state in ^{50}Fe, although with a large uncertainty [22]. Combined with our shell-model calculations using well-developed effective nucleon-nucleon interactions, the present data allow us to carry out a comparative study of the measured and calculated EM transition rates in the $A = 50$, $N \sim Z$ isobaric triplet.

II. EXPERIMENTAL DETAILS

Excited states in ^{50}Mn/^{50}Cr were populated using the ^{40}Ca(^{12}C,pn/2p) fusion-evaporation reaction in a chamber housing the Cologne plunger device [23] at the FN Tandem facility of the University of Cologne. A 30.5-MeV ^{12}C beam of ∼5-pnA current bombarded a 0.5-mg/cm^2 ^{40}Ca target for ten days. The target foil had a ^{197}Au layer with a thickness of ∼2 mg/cm^2 on the upstream side and ∼0.1 mg/cm^2 on the downstream side to protect it from oxidation. To detect γ rays from the reaction products, the chamber was surrounded by 11 germanium detectors that were placed at a distance of ∼12 cm from the center of the ^{40}Ca target. The arrangement resulted in two rings of detectors, namely, Ring(1) at $\theta = 142.3^\circ$ and Ring(2) at $\theta = 45.0^\circ$ with respect to the beam axis, consisting of five and six detectors, respectively. An additional detector, referred to as Ring(3), was placed at a similar distance from the target at $\theta = 0^\circ$. Data from all of the detectors were recorded with time stamps using a 80-MHz clock. The ^{12}C beam energy was varied between 30 and 36 MeV [18,24] and the observed intensity of the 343-keV $3^+ \rightarrow 2^+$ γ-ray transition in ^{50}Mn was used to conclude that a beam energy of 30.5 MeV would be optimal. The ^{50}Mn and ^{50}Cr recoils had velocities of $v \sim 1\% \times c$ after leaving the ^{40}Ca target (see Table I) and were stopped in a ^{181}Ta foil (stopper) with a thickness of ∼3.5 mg/cm^2. Here, c is the speed of light. These two velocity regimes resulted in a Doppler-shifted (referred to as fully shifted) peak and an unshifted peak with corresponding intensity components of I^s and I^{us} for a given γ-ray transition of interest in an energy spectrum. The "target-to-stopper" (plunger) distances x were chosen so as to cover the expected "region of sensitivity" for a measurement of the lifetime of the 2^+ state in ^{50}Cr [23]. In this region, there was a significant variation in $I^s(x)$ as a function of x both for the 783- and 800-keV γ rays from the decays of the 2^+ states in ^{50}Cr and ^{50}Mn, respectively (cf. Fig. 1). This allowed for lifetime measurements for these states in the same experiment. Table I gives the ten plunger distances used in the present work. The procedure used to calculate the effective velocities v_{eff}, as well as the effective distances x_{eff} corresponding to the ^{50}Cr and ^{50}Mn recoils, which are required to perform the lifetime analysis, is discussed below (cf. Sec. III). Data were collected for ∼12 hours at each distance and were analyzed using the differential decay curve method (DDCM) within the recoil distance Doppler-shift (RDDS) technique [23,25,26].

III. ANALYSIS AND RESULTS

Data were sorted offline using the SOCO2 software package [27]. Peaks with widths of $t_p \sim 500$ ns were observed in $\gamma\gamma$ time-difference (timing) spectra, corresponding to prompt γ rays at the target position. Therefore, time windows with widths of $t_{bl} \sim t_{br} \sim 250$ ns on the left (l) and the right (r) sides of this peak were used for background subtraction purposes. Ring(i) versus Ring(j) $\gamma\gamma$ energy matrices were thus constructed using the above values of t_p, t_{bl}, and t_{br}. Here, i and j can take values of 1, 2, and 3, representing the three rings in the present setup. A $\gamma\gamma$-coincidence analysis was performed using the RADWARE package [28].

Figure 2(a) shows the Ring(1) γ-ray spectrum that was obtained by taking the total projection of the Ring(1) versus Ring(2) $\gamma\gamma$ energy matrix constructed using all of the data collected at all of the plunger distances. The observed γ rays mainly belong to ^{50}Cr and ^{50}Mn. A few γ decays in ^{181}Ta, originating from the inelastic scattering of the beam, were also observed. Figure 2(b) shows a Ring(1) γ-ray spectrum gated by the $(3^+ \rightarrow 2^+)$ 343-keV transition in ^{50}Mn observed in Ring(2). As can be seen, the γ rays originating from ^{50}Mn are relatively enhanced. In Fig. 2(c), a similar spectrum gated by the $(4^+ \rightarrow 2^+)$ 1098-keV transition in ^{50}Cr shows γ rays mainly from ^{50}Cr. Figure 3 shows partial level schemes of ^{50}Mn and ^{50}Cr nuclei deduced from an analysis of the present data. Only low-lying levels were populated in ^{50}Mn. This can be attributed to the lower beam energy (or lower excitation energy of the compound nucleus) and to the more asymmetric reaction (or lower grazing angular momentum) used in the present work in comparison with that of the previous works [6]. Consequently, higher-lying states are expected to have a weak (or no) influence on the population of the first 2^+state, allowing a reliable lifetime analysis.

TABLE I. A table of physical distances (x) between the target and the stopper, the normalized intensities of the fully shifted [$I^s \equiv \{I^s_A, I^s_B\}(x)$] and the unshifted [$I^{us} \equiv \{I^s_A, I^{us}_B\}(x)$] components of B in coincidence with the fully shifted component of A, the energy shift in the fully shifted peak for Ring(1) (ΔE) and the effective velocity of the recoils at a given distance ($v_{\rm eff}$ relative to the speed of light). $x_{\rm eff}$ is calculated using $v_{\rm eff}$ (see the text for details).

x (μm)	$\{I^s_{343}, I^s_{800}\}$	$\{I^s_{343}, I^{us}_{800}\}$	$\Delta E^{\rm Mn}_{800}$(keV)	$\frac{v^{\rm Mn}_{\rm eff}}{c}$(%)	$x^{\rm Mn}_{\rm eff}$ (μm)	$\{I^s_{1098}, I^s_{783}\}$	$\{I^s_{1098}, I^{us}_{783}\}$	$\Delta E^{\rm Cr}_{783}$ (keV)	$\frac{v^{\rm Cr}_{\rm eff}}{c}$(%)	$x^{\rm Cr}_{\rm eff}$ (μm)
20.8(2)	1793(59)	1177(44)	6.10(5)	0.963(6)	20.8(2)	24698(450)	69421(1290)	5.32(3)	0.864(3)	20.8(2)
26.8(2)	1895(62)	1085(33)	6.29(7)	0.995(10)	25.9(3)	30205(512)	73706(1220)	5.47(5)	0.888(7)	26.0(3)
29.7(2)	2257(78)	920(47)	6.30(11)	0.995(13)	28.8(3)	33712(821)	68149(1450)	5.55(7)	0.902(9)	28.5(3)
33.8(2)	2325(57)	845(34)	6.27(8)	0.990(11)	32.9(3)	37980(560)	67395(828)	5.64(5)	0.917(6)	31.8(3)
38.8(2)	2515(57)	655(26)	6.40(11)	1.010(13)	37.0(3)	45965(751)	61752(950)	5.82(5)	0.945(7)	35.4(3)
48.8(2)	2689(72)	386(28)	6.48(9)	1.024(11)	45.9(3)	59841(974)	49474(769)	5.94(5)	0.966(7)	43.6(3)
58.8(2)	2869(78)	325(27)	6.61(7)	1.044(9)	54.2(4)	69215(1167)	41369(719)	6.17(6)	1.003(7)	50.6(4)
68.8(2)	2949(89)	290(32)	6.64(6)	1.049(8)	63.1(4)	79940(1411)	32012(579)	6.19(3)	1.006(4)	59.0(4)
78.8(2)	2928(77)	121(20)	6.71(6)	1.060(8)	71.6(4)	86324(1594)	25621(553)	6.32(3)	1.028(4)	66.2(4)
166.8(2)	3261(147)	7(24)	6.76(6)	1.067(7)	150.5(8)	109442(2081)	5457(390)	6.51(2)	1.059(3)	136.0(8)

Among all of the possible Ring(i) versus Ring(j) $\gamma\gamma$ energy matrices, the Ring(1) versus Ring(2) matrix was found to be the best choice for a clean lifetime analysis. Specifically, in the Ring(1) γ-ray energy spectra, γ-ray transitions from contaminants do not appear in the vicinity of the 800-keV line, corresponding to the decay of the 2^+ state in ^{50}Mn. For all of the other choices of matrices, contaminants overlapped with the γ-ray peaks of interest; therefore, those matrices were not used in the lifetime analysis. Figure 4 presents

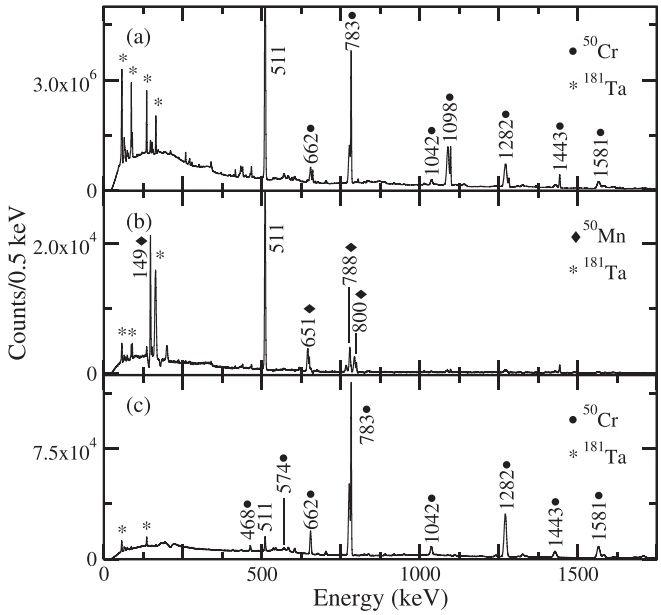

FIG. 2. γ-ray energy spectra of Ring(1), showing the total statistics collected for all of the distances given in Table I. The histograms were obtained by utilizing the Ring(1) versus Ring(2) $\gamma\gamma$ energy matrix and (a) taking the total projection, (b) gating with the 343-keV line corresponding to the $3^+ \rightarrow 2^+$ γ decay in ^{50}Mn, and (c) gating with the 1098-keV line corresponding to the $4^+ \rightarrow 2^+$ γ decay in ^{50}Cr. The 610-keV transition is known to be much weaker compared to the 662-keV transition, therefore, was not prominent in the spectra [18].

Ring(1) γ-ray spectra for all ten distances, x. The region relevant to the fully shifted and unshifted components of the $2^+ \rightarrow 0^+$ 783-keV transition in ^{50}Cr is shown. These histograms are gated by the fully shifted peak of the 1098-keV γ ray, corresponding to the $4^+ \rightarrow 2^+$ transition in ^{50}Cr [cf. Fig. 3(b)], in the Ring(2) γ-ray spectrum. High statistics and a clear separation between the fully shifted and unshifted peaks allowed us to perform an accurate lifetime analysis. Table I gives the normalized intensities, $I^{us} \equiv \{I^s_{1098}, I^{us}_{783}\}(x)$ and $I^s \equiv \{I^s_{1098}, I^s_{783}\}(x)$. Here, $\{I^s_A, I^{us}_B\}$ is the intensity of the unshifted component of B in coincidence with the fully shifted component of A. To extract I^s, Gaussian fits were performed by leaving the width and centroid parameters free. In the case of the unshifted peaks, these two parameters are not expected to change with x. Therefore, they were fixed to be the values obtained with the data collected at $x = 20.8\,\mu$m.

The lifetime of the 2^+ state in ^{50}Cr was determined in the standard DDCM [23] by using

$$\tau_{2^+}(x) = -\frac{1}{v}\frac{\{I^s_{1098}, I^{us}_{783}\}(x)}{\frac{d}{dx}\{I^s_{1098}, I^s_{783}\}(x)}.$$

First, $\tau_{2^+}(x)$ was obtained from a piecewise fit to the fully shifted peak intensities, i.e., $\{I^s_{1098}, I^s_{783}\}(x)$ [29]. Final values of τ_{2^+} were then determined by using a χ^2 minimization procedure to fit $\{I^s_{1098}, I^{us}_{783}\}(x)$ to the derivative of this piecewise-fitted function multiplied by $v\tau_{2^+}(x)$. The computer code NAPATAU [29] was used for this purpose. A weighted average of $\tau_{2^+}(x)$ values within the "region of sensitivity" gives the measured lifetime τ_{2^+} of the first 2^+ state in ^{50}Cr. The influence of the side-feeding on the lifetime result is avoided by gating directly above on the fully shifted peak of the 1098-keV γ ray feeding the 2^+ state and analyzing I^s and I^{us} for the 783-keV γ ray [23]. The uncertainty in τ^+_2 has contributions from statistics, branching ratios, normalization procedure, distances, and recoil velocities, some of which are discussed below.

The intensities I^s and I^{us} were normalized to correct for differences in the total number of beam particles for the measurements carried out at different x. Three choices were

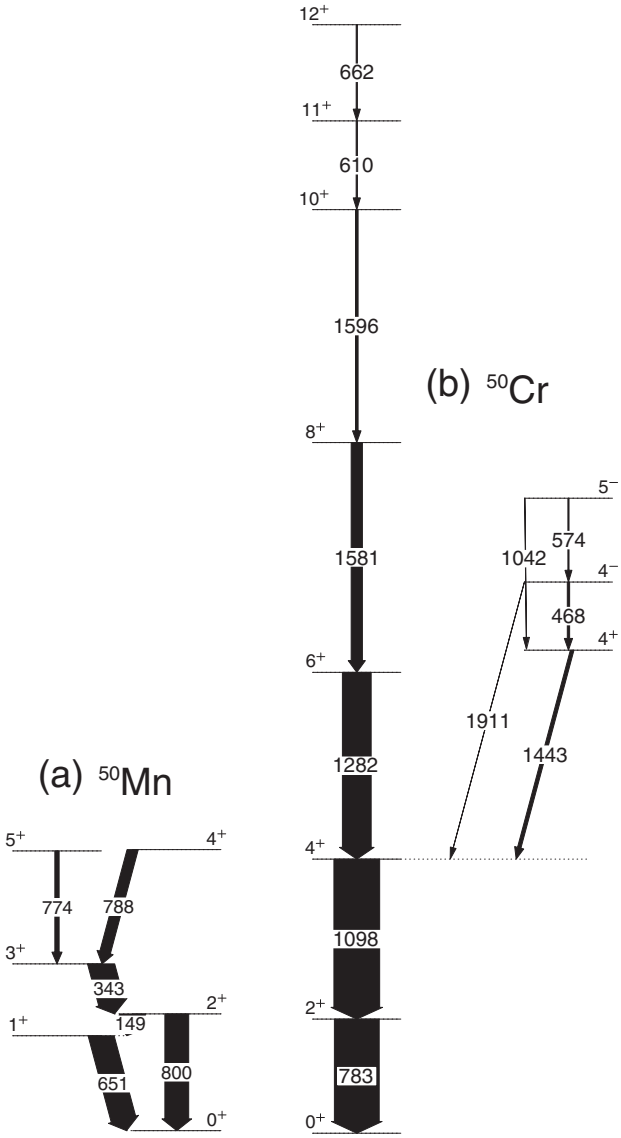

FIG. 3. Partial level schemes of (a) ^{50}Mn and (b) ^{50}Cr obtained from the present data. Only decays from low-lying states with spins $\leqslant 5$ can be seen in ^{50}Mn due to much lower cross sections compared to ^{50}Cr.

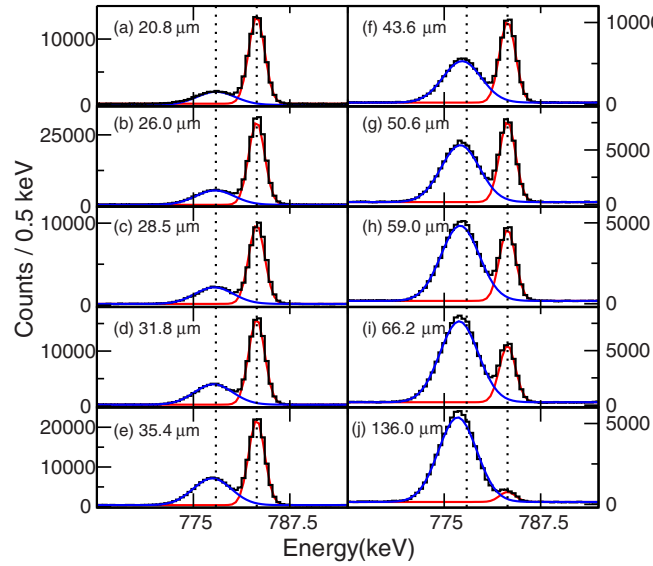

FIG. 4. γ-ray energy spectra of Ring(1) showing the fully shifted and the unshifted peaks corresponding to the 783-keV γ-ray transition in ^{50}Cr. The histograms were obtained by utilizing the Ring(1) versus Ring(2) $\gamma\gamma$ energy matrix and gating with the fully-shifted peak of the $4^+ \rightarrow 2^+$ 1098-keV transition on the Ring(2) axis. Each of the spectra [from (a) to (j)] is labeled with the effective plunger distance $x_{\text{eff}}^{\text{Cr}}$. The dotted lines corresponds to the centroids of fully shifted and unshifted peaks of the 783-keV γ-ray at $x_{\text{eff}}^{\text{Cr}} = 20.8\,\mu$m.

investigated, namely, (i) the total counts in the Ring(1) γ-ray energy spectra that were obtained by taking the total projections of the Ring(1) versus Ring(2) matrices, (ii) the intensities of the γ-ray transitions in ^{181}Ta, and (iii) the intensities of the γ-ray transitions in ^{50}Cr [26]. In any case, the lifetime results obtained using the three different normalization methods were found to be consistent with each other within the uncertainties. In the method (iii), the statistics were sufficiently large and no systematic trend was present in $\tau(x)$ as a function of x. This indicates that the systematic error due to the presence of any contaminant nuclei was minimized. Therefore, the method (iii) proved to be the most reliable one. It also avoids systematic uncertainties arising from the presence of activation γ-rays in the energy spectra used in the method (i).

Figure 5 presents an analysis, using NAPATAU, of $I^s(x_{\text{eff}})$ and $I^{\text{us}}(x_{\text{eff}})$ for the 783-keV γ ray given in Table I. The measurement at $x_{\text{eff}}^{\text{Cr}} = 20.8\,\mu$m is not considered due to the unphysical gradients observed for $I^s(x)$ and $I^{\text{us}}(x)$, which might have originated from a relatively high systematic uncertainty for this smallest plunger distance. A lifetime value of 13.3(6) ps was thus obtained for the 2^+ state in ^{50}Cr. This result is in a very good agreement with the published values of 12.8(7) ps [16,17] and 13.2(4) ps [19], indicating an absence of any significant systematic errors in the present measurements. As shown in Fig. 6, a similar analysis for the 4^+ state in ^{50}Cr gives a lifetime of 4.9(7) ps, which is consistent with the previously measured values of 3.2(4) ps [16,17] and 3.2(7) ps [19]. The ratio

$$B_{4/2} = \frac{B(E2: 4^+ \rightarrow 2^+)}{B(E2: 2^+ \rightarrow 0^+)} = \frac{\tau_{2^+} E_\gamma^5(2^+ \rightarrow 0^+)}{\tau_{4^+} E_\gamma^5(4^+ \rightarrow 2^+)}$$

is calculated to be 0.50(8) using our results [30,31]. Here E_γ is the energy of the γ-ray transition. This result is in disagreement with the expected values of $\sim$1.4 for a rotational nucleus and of $\sim$2 for a vibrational nucleus. The calculated ratios using the available data for ^{50}Cr varied between 0.7 to 1.13 [16,17,19,30,32]. Clearly, the $B_{4/2}$ value in ^{50}Cr is found to be much less than 1 in the present work. Currently, this result is considered to be anomalous and cannot be explained by theoretical models [30,31]. It adds to such data available for nuclei in the $A \sim 50$, 70, 110, and 160 regions, which will serve as a testing ground for new calculations with modified models in the future [33,34].

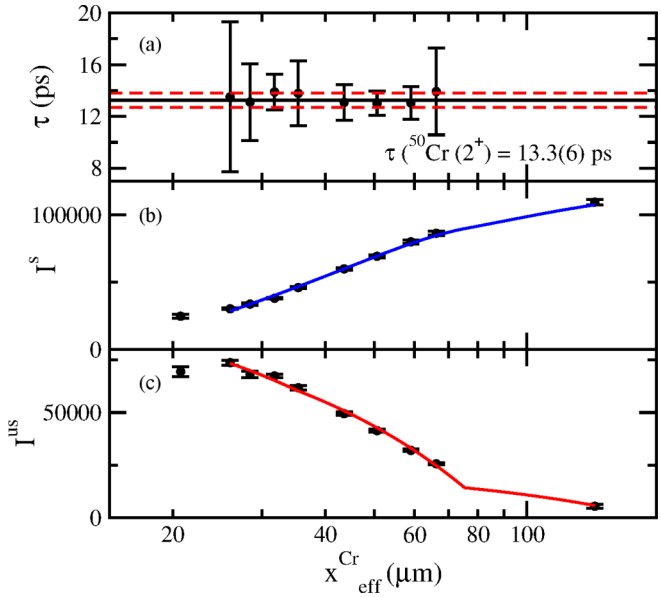

FIG. 5. An analysis of the intensities of the 783-keV γ-ray given in Table I to obtain the lifetime of the 2^+ state in ^{50}Cr. (a) The individual lifetimes obtained at eight distances in the "region of sensitivity" are shown. The final result from a weighted average is also given. The intensities, I^s and I^{us}, are shown as a function of distance in (b) and (c), respectively, along with the best fits (solid lines) obtained using NAPATAU [29].

Figure 7 shows the Ring(1) γ-ray spectra gated by the fully shifted peak of the $3^+ \rightarrow 2^+$ 343-keV decay in ^{50}Mn [cf. Fig. 3(a)], observed in the Ring(2) γ-ray spectra. The region relevant to the $2^+ \rightarrow 0^+$ 800-keV transition in ^{50}Mn is shown for all x with the clearly separated fully shifted and unshifted peaks. The values of I^s and I^{us} for the 800-keV line, obtained from these spectra, are given in Table I. Figure 8 shows an analysis using NAPATAU, resulting in a lifetime value of $\tau(^{50}\text{Mn}(2^+)) = 6.4(2)$ ps.

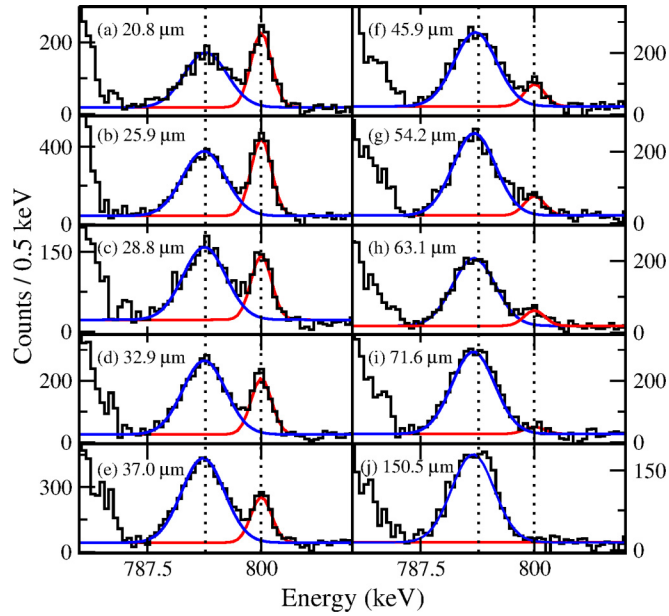

FIG. 7. Similar to Fig. 4, γ-ray energy spectra gated by the fully shifted peak of the $3^+ \rightarrow 2^+$ 343-keV transition in ^{50}Mn, showing the fully shifted and unshifted peaks of the 800-keV γ-ray.

It is evident from Figs. 4 and 7 that there is a systematic variation in the centroid of the fully shifted peak as a function of x, similar to that discussed in Ref. [35]. This can be understood in terms of the recoil-velocity distribution corresponding to the fully shifted peak. In particular, the effect arises because the relation of the recoil velocity with flight time (or x) between the foils is linear while it is exponential between I^s and x. In other words, the γ-ray intensities in the

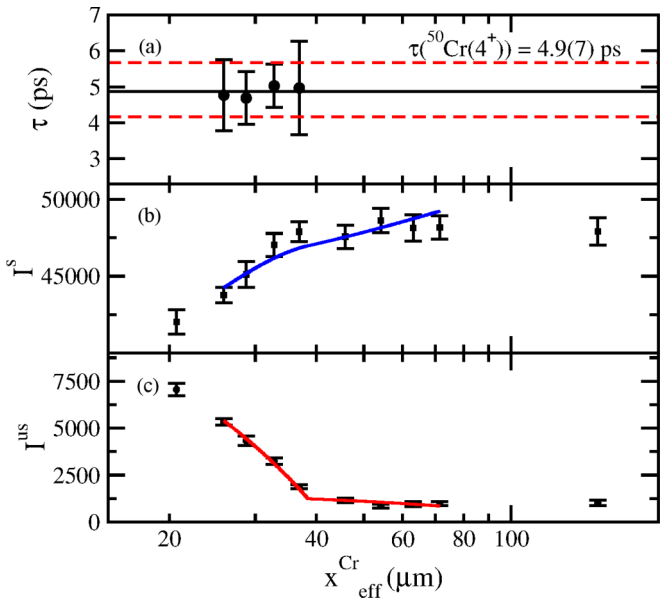

FIG. 6. Same as Fig. 5 for the 4^+ state in ^{50}Cr.

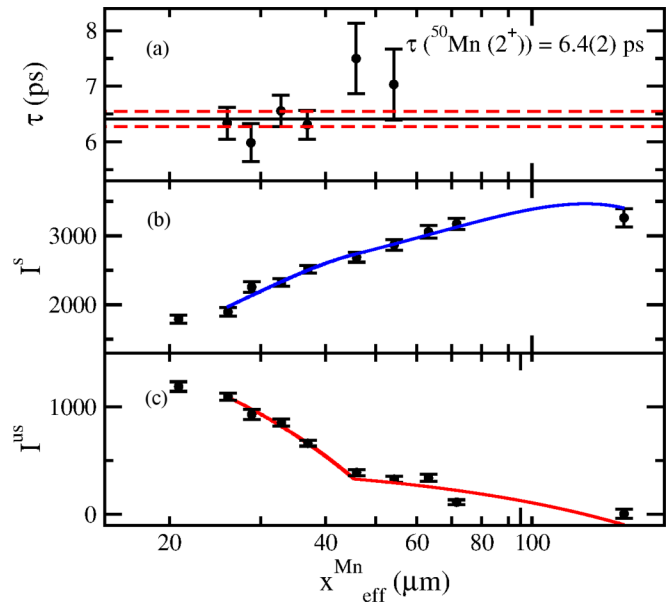

FIG. 8. Same as Fig. 5 for the 2^+ state in ^{50}Mn.

fully shifted peaks have more contributions from slower recoils at smaller distances. To account for this, first the Doppler shift observed for the 800-keV $2^+ \rightarrow 0^+$ γ-ray transition in ^{50}Mn was obtained at $x \sim 20.8\,\mu$m. The corresponding effective velocity of the recoils ($v^{\rm rec}$) was then deduced by using $|\Delta E_\gamma| = (v^{\rm rec}/c) \times \cos\theta$. Here θ is the angle of the ring of γ-ray detectors with respect to the beam direction. This effective recoil velocity ($v^{\rm rec}_{\rm eff}$) at $\sim$20.8 μm was fixed to be the "nominal recoil velocity" ($v^{\rm rec}_{\rm nom}$). Differences between $v^{\rm rec}_{\rm nom}$ and $v^{\rm rec}_{\rm eff}(x)$ at all of the other x values, $dv^{\rm rec}(x) = v^{\rm rec}_{\rm nom} - v^{\rm rec}_{\rm eff}(x)$, were then obtained by using the correspondingly observed Doppler shifts for the 800-keV γ ray. As shown in Table I for the case of ^{50}Mn, a systematic change in the effective recoil velocity from $v^{\rm Mn}_{\rm eff}/c \sim 0.96$ % (around 20 μm) to $\sim$1.07 % (170 μm) was observed as a function of x. The effective plunger distances ($x^{\rm rec}_{\rm eff}$), corresponding to $v^{\rm rec}_{\rm nom}$, were then obtained by correcting the original plunger distances with the flight path corresponding to $dv^{\rm rec}(x)$. A similar analysis was also performed for the 783-keV $2^+ \rightarrow 0^+$ γ decay in ^{50}Cr. The x and $x^{\rm rec}_{\rm eff}$ corresponding to these recoil nuclei are presented in Table I. This last was used for the lifetime analysis performed using NAPATAU. Slight differences between the effective velocities of ^{50}Mn and ^{50}Cr recoils can be noted from the table. This is not surprising because these nuclei were produced in two different (pn and $2p$) reaction channels with a broader velocity distribution for ^{50}Cr recoils. In addition, the corresponding 2^+ states have significantly different lifetimes, leading to a larger x range for $I^{\rm us}/I^{\rm tot}$ in the case of ^{50}Cr compared to that for ^{50}Mn. Monte Carlo simulations [36] were performed to understand the effective recoil velocity as a function of distance. The variations in centroids observed in Figs. 4 and 7 could be reproduced when the thickness of the ^{40}Ca target-foil was set to be 0.65 mg/cm^2. This is different from the quoted value of 0.50 mg/cm^2, which could have been underestimated. It is also possible that the recoils traveled through the ^{197}Au layer that was thicker than 0.1 mg/cm^2, the effect of which could not be disentangled unambiguously from the effect of the difference in the target thickness. In summary, simulations using slightly higher overall foil thickness traversed by the recoils reproduce the observed systematic trends in the centroids of the fully shifted peak.

IV. DISCUSSION

The $B(E2\downarrow: 2^+ \rightarrow 0^+)$ value of 237(8) e^2fm^4 for ^{50}Mn obtained from the present work is given in Table II together with the known value for ^{50}Fe [22]. To calculate the $B(E2)$ value from the measured lifetime of the first 2^+ state in ^{50}Mn, the relative intensities of 64.1(12) and 100(2) were used for the 149 and 800 keV γ-decays, respectively [37]. The $B(E2)$ value presented for ^{50}Cr is a weighted average of the data from the present and previous works [16,17,19]. The experimental values are compared to our theoretical predictions obtained using the shell-model code ANTOINE [38] in the full pf space. Two sets of calculations are given in Table II. The $B(E2)_{gxc}$ values were predicted using the GXPF1A effective interaction [39] plus the Coulomb matrix elements obtained in the harmonic oscillator basis with single-particle energy corrections following Ref. [2] and the standard effective charges of $e_\pi = 1.5$ and $e_\nu = 0.5$. In the case of $B(E2)_{kbc}$, the KB3GR effective interaction has been used [40] together with $e_\pi = 1.31$ and $e_\nu = 0.46$ [41]. The Coulomb matrix elements were obtained in the same way as for the other calculation, but with the single-particle energy corrections that reproduce the experimental energies in ^{41}Ca and ^{41}Sc. The $B(E2)_{gx}$ values calculated using the GXPF1A effective interaction and without the Coulomb matrix elements are also reported for comparison. Figure 9 summarizes $M(E2) = \sqrt{B(E2\uparrow: 0^+ \rightarrow 2^+)}$ values for the $A = 50$, $T = 1$ triplet, presenting the current status of the agreement between the data and the calculations. Both of the calculations reproduce the data for the triplet with good accuracy. The shell-model values follow a rather linear and slightly increasing behavior with Z for the $M(E2)$ matrix element, which is fully consistent with the data. However, the high uncertainty in the measurement of ^{50}Fe precludes a final conclusion. The calculations

TABLE II. A comparison between data and shell-model predictions of the $B(E2)$ values for the $A = 50$, $T = 1$ triplet. Here gxc and kbc correspond to the calculations carried out using the GXPF1A and the KB3GR interactions, respectively, that include Coulomb matrix elements while gx corresponds to the prediction without Coulomb contribution and using the GXPF1A interaction (see text for details).

Nucleus	$E(2^+)_{ex}$ (keV)	$E(2^+)_{gxc}$ (keV)	$B(E2)_{ex}$ (e^2fm^4)	$B(E2)_{gxc}$ (e^2fm^4)	$B(E2)_{gx}$ (e^2fm^4)	$B(E2)_{kbc}$ (e^2fm^4)
^{50}Fe	765	779	281(61)	217	225	201
^{50}Mn	800	796	237(8)	214	221	200
^{50}Cr	783	784	211(4)	211	217	196

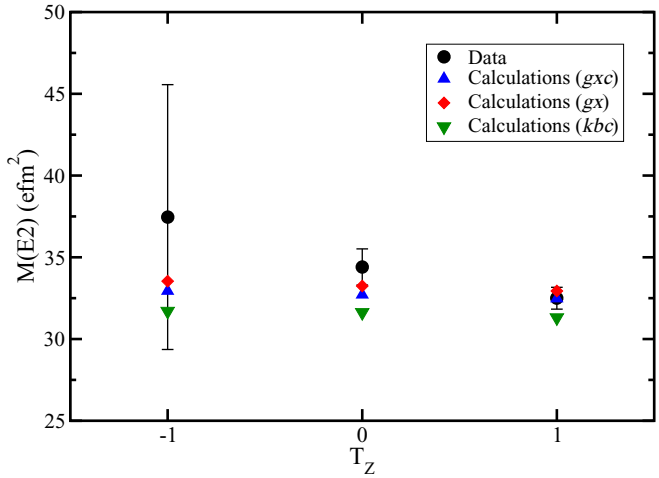

FIG. 9. The matrix element $M(E2)$ as a function of T_z for the three $T = 1$, $A = 50$ isobaric nuclei. Datum for ^{50}Mn was obtained for the first time in the present work. In the case of ^{50}Cr, the data point is a weighted average of our result and that from Refs. [16,17,19] while the result from Ref. [22] has been used for the case of ^{50}Fe with $T_z = -1$. The predictions from our calculations are also shown (see the text for details).

suggest a very small isospin mixing, as the nondiagonal Coulomb matrix elements are of the order of a few tens of keV. A more precise determination of the $B(E2)$ value in ^{50}Fe would allow for more definitive conclusions on the presence or absence of a nonlinear dependence of the matrix element with T_z.

V. CONCLUSION

The lifetimes of the $T = 1$ isobaric analog 2^+ states in ^{50}Cr and ^{50}Mn are measured in the same experiment using the plunger technique. The present value for ^{50}Cr agrees with that from the previous measurements, providing confidence in the new result obtained for ^{50}Mn. Both the data and the predictions from the large-scale shell-model calculations exhibit a rather linear and slightly increasing behavior of the $M(E2)$ matrix element with Z for the $A = 50$, $T = 1$ isobaric triplet. At present, the value available for the proton-rich ^{50}Fe nucleus has a very large uncertainty and a high precision measurement is required to draw definite conclusions on isospin-symmetry breaking in this triplet.

ACKNOWLEDGMENTS

We gratefully acknowledge the support of accelerator staff and the students at the FN Tandem facility of the University of Cologne. We would like to thank Prof. Robert Chapman and Prof. John F. Smith for the help at the final stages of this manuscript. M.M.G., B.S.N.S., L.B., D.M.C., and M.M. acknowledge support of the Science and Technology Facilities Council, Grant No. ST/L005794/1. M.B., A.B., T.B., A.D., A.G., C.F., J.J., F.M., C.M., D.W., and K.O.Z. were funded by the German Ministery of Science and Education (BMBF), Grant No. 05P15PKFNA. A.P. was partially supported by MINECO (Spain) Grant No. FPA2014-57196, the Severo Ochoa Programme SEV-2016-0597.

[1] P. Baczyk *et al.*, Phys. Lett. B **778**, 178 (2018).
[2] M. A. Bentley and S. M. Lenzi, Prog. Part. Nucl. Phys. **59**, 497 (2007).
[3] D. D. Warner *et al.*, Nat. Phys. **2**, 311 (2006).
[4] S. M. Lenzi *et al.*, Phys. Rev. Lett. **87**, 122501 (2001).
[5] P. J. Davies *et al.*, Phys. Rev. Lett. **111**, 072501 (2013).
[6] C. D. O'Leary *et al.*, Phys. Lett. B **525**, 49 (2002).
[7] S. A. Milne *et al.*, Phys. Rev. Lett. **117**, 082502 (2016).
[8] J. Henderson *et al.*, Phys. Rev. C **90**, 051303(R) (2014).
[9] B. S. Nara Singh *et al.*, Phys. Rev. C **75**, 061301(R) (2007).
[10] A. P. Zuker, S. M. Lenzi, G. Martínez-Pinedo, and A. Poves, Phys. Rev. Lett. **89**, 142502 (2002).
[11] L. A. Radicati, Phys. Rev. **87**, 521 (1952); and the references therein.
[12] F. M. Prados Estevez *et al.*, Phys. Rev. C **75**, 014309 (2007); and the references therein.
[13] P. Van Isacker, Rep. Prog. Phys. **62**, 1661 (1999).
[14] G. Colo, M. A. Nagarajan, P. VanIsacker, and A. Vitturi, Phys. Rev. C **52**, 1175(R) (1995).
[15] A. Petrovici, Phys. Rev. C **91**, 014302 (2015).
[16] L. K. Peker, Nucl. Data Sheets **68**, 271 (1993); T. W. Burrows, *ibid.* **68**, 1 (1993); **75**, 1 (1995); H. Junde, *ibid.* **71**, 659 (1994).
[17] F. Brandolini *et al.*, Nucl. Phys. A **642**, 387 (1998).
[18] N. Pietralla *et al.*, Phys. Rev. C **65**, 024317 (2002).
[19] R. Ernst *et al.*, Phys. Rev. C **62**, 024305 (2000); R. Ernst, Phys. Rev. Lett. **84**, 416 (2000); and http://www.nndc.bnl.gov/ensdf/.
[20] M. A. Bentley (private communication).
[21] K. Jessen, O. Moller, A. Dewald, P. vonBrentano, A. Fitzler, J. Jolie, B. Saha, P. Petkov, F. Brandolini, A. Gadea, S. M. Lenzi, G. deAngelis, E. Farnea, D. R. Napoli, and B. J. P. Gall, Phys. Rev. C **74**, 021304(R) (2006).
[22] K. Yamada *et al.*, Eur. Phys. J. A **25**, 409 (2005); and http://www.nndc.bnl.gov/ensdf/.
[23] A. Dewald, O. Moller, and P. Petkov, Prog. Part. Nucl. Phys. **67**, 786 (2012).
[24] C. W. Beausang *et al.*, Nucl. Instrum. Methods Phys. Res., Sect. A **452**, 431 (2000).
[25] A. Dewald, S. Harissopulos, and P. von Brentano, Z. Phys. A **334**, 163 (1989).
[26] D. Hodge *et al.*, Phys. Rev. C **94**, 034321 (2016).
[27] The SOCO software package developed by nuclear physics group of The University of Cologne, N. Saed-Samii, Diploma Thesis (2013).
[28] D. C. Radford, Nucl. Instrum. Methods Phys. Res., Sect. A **361**, 297 (1995).
[29] G. Böhm, A. Dewald, P. Petkov, and P. von Brentano, Nucl. Instrum. Methods Phys. Res., Sect. A **329**, 248 (1993).
[30] D. Hertz-Kintish, L. Zamick, and S. J. Q. Robinson, Phys. Rev. C **90**, 034307 (2014).
[31] B. Cederwall *et al.*, Phys. Rev. Lett. **121**, 022502 (2018).
[32] F. Brandolini *et al.*, Phys. Rev. C **70**, 034302 (2004).
[33] B. Saygi *et al.*, Phys. Rev. C **96**, 021301(R) (2017).
[34] R. B. Cakirli, R. F. Casten, J. Jolie, and N. Warr, Phys. Rev. C **70**, 047302 (2004).
[35] K. Arnswald *et al.*, Phys. Lett. B **772**, 599 (2017).
[36] T. Braunroth, Ph.D. Thesis (2017), https://kups.ub.uni-koeln.de/7956/1/Braunroth_Dissertation_pub.pdf.
[37] A. Schmidt, I. Schneider, C. Friessner, A. F. Lisetskiy, N. Pietralla, T. Sebe, T. Otsuka, and P. von Brentano, Phys. Rev. C **62**, 044319 (2000).
[38] E. Caurier and F. Nowacki, Acta. Phys. Pol. B **30**, 705 (1999).
[39] M. Honma, T. Otsuka, B. A. Brown, and T. Mizusaki, Phys. Rev. C **65**, 061301(R) (2002).
[40] E. Caurier and A. Poves (unpublished).
[41] M. Dufour and A. P. Zuker, Phys. Rev. C **54**, 1641 (1996).